

Optical chirality of membrane metasurfaces with broken in-plane symmetry

Ivan Toftul,^{1,*} Brijesh Kumar,^{1,2,†} Maxim Gorkunov, and Yuri Kivshar¹

¹Research School of Physics, Australian National University, Canberra ACT 2601, Australia

²Department of Physics, Indian Institute of Technology Bombay, Mumbai 400076, India

(Dated: June 5, 2026)

We study chiroptical properties of single-layer dielectric membrane metasurfaces with broken in-plane symmetry. In sharp contrast to a common belief that chiral optical phenomena require symmetry breaking in the vertical direction, we show that flat single-layer metasurfaces are capable of strong specific chiral effects. Although the single-layer geometry forbids conventional co-polarized circular dichroism, strong resonant conversion circular dichroism appears to be possible in particular wavelength ranges determined by the spectra of photonic eigenmodes. We explore its origin starting with a C_4 rotation-symmetric and in-plane mirror-symmetric membrane metasurface and applying to it various in-plane perturbations. Simultaneously breaking of the in-plane mirror symmetry and lifting the rotation symmetry unlocks resonantly enhanced circular conversion dichroism. We derive selection rules for this effect and trace its origin to eigenmode interference and intercoupling using chiral coupled-mode theory.

I. INTRODUCTION

Chirality, in its geometric sense, indicates non-identity of an object and its mirror image [1]. Optical chirality is a much more specific property which can be precisely quantified by the dissymmetry of interactions with circularly polarized light. Historically, chiral optical phenomena are largely attributed to geometric chirality [2, 3]. Thus a differential optical response of chiral enantiomer solutions to left and right circularly polarized (LCP and RCP) light is generally referred to as *circular dichroism* (CD) manifesting itself through dissymmetry of absorption, reflection and transmission of layers or interfaces [4], as well as of scattering cross sections of compact single objects [5].

Artificial chiral electromagnetic materials have evolved from upscale models explaining the origin of natural optical chirality [6, 7]. Nowadays, as the demand for sources, detectors, filters, and sensors of chiral light is growing, compact chiral optical elements are extensively studied. Here the concept of chiral metasurfaces – two-dimensional subwavelength arrays of chiral meta-atoms – attracts significant attention. Such metasurfaces built of meta-atoms of high refractive index transparent materials demonstrate strongly chiral high-quality factor (high-Q) resonances underpinned by specific photonic eigenmodes [8–10].

While the shapes of meta-atoms can be relatively simple, the in-plane mirror symmetry can be broken by multiple means: from breaking symmetry on the meta-atom level [11], rotation of simple shapes relative to the lattice arrangement [12, 13], monoclinic lattice arrangement [14], as well as using anisotropic materials by achieving a mismatch between the optical axis and the lattice arrangement [15, 16]. The out-of-plane (vertical) mirror symmetry is broken by different heights [8, 17–19] or by a lateral tilt [20, 21]. Although in some cases, this symmetry breaking can be more subtly produced by a substrate [14, 22] or adjacent layers [23, 24],

the resulting chiral optical phenomena are all determined by the fully broken mirror symmetry. The main effect in transmission is then designated by the co-polarized circular dichroism:

$$CD_{co} = \frac{T_{RR} - T_{LL}}{T_{RR} + T_{LL}}. \quad (1)$$

The energy transmission coefficients T here are defined in the basis of circular polarizations with the second index denoting the polarization of the incident wave and the first one – the polarization of the outgoing transmitted wave. Note that even for a geometrically chiral metasurface CD_{co} (1) can vanish if it possesses a rotation symmetry of the order 3 or higher and its materials are reciprocal and not sufficiently strongly light absorbing [23, 25].

At the same time, it is regularly noted that certain chiral optical phenomena can be present in flat metasurfaces retaining their out-of-plane mirror symmetry [26–28]. Being geometrically achiral, such structures are incapable of conventional CD_{co} , but they can perform as resonant chiral mirrors reflecting waves of one helicity and transmitting the others while fully flipping their helicity. This type of chiral optical dissymmetry is known as *circular conversion dichroism* [29] defined similarly to Eq. (1) as:

$$CD_{cross} = \frac{T_{RL} - T_{LR}}{T_{RL} + T_{LR}}. \quad (2)$$

For applications involving chiral light manipulations, the transmittance difference:

$$\Delta T_{cross} = T_{RL} - T_{LR}, \quad (3)$$

is more relevant.

Note that although circular polarization conversion is generally performed also by birefringent objects (e.g. half-wave plates), for them always $\Delta T_{cross} = 0$. Early plasmonic metamaterial-based designs have demonstrated the possibility of imbalance between the conversion directions [29–31]. Dielectric-based designs less suffering from absorption losses emerged almost a decade later [13, 26, 28, 32, 33].

* toftul.ivan@gmail.com; equal contribution

† Brijesh.Kumar@iitb.ac.in; equal contribution

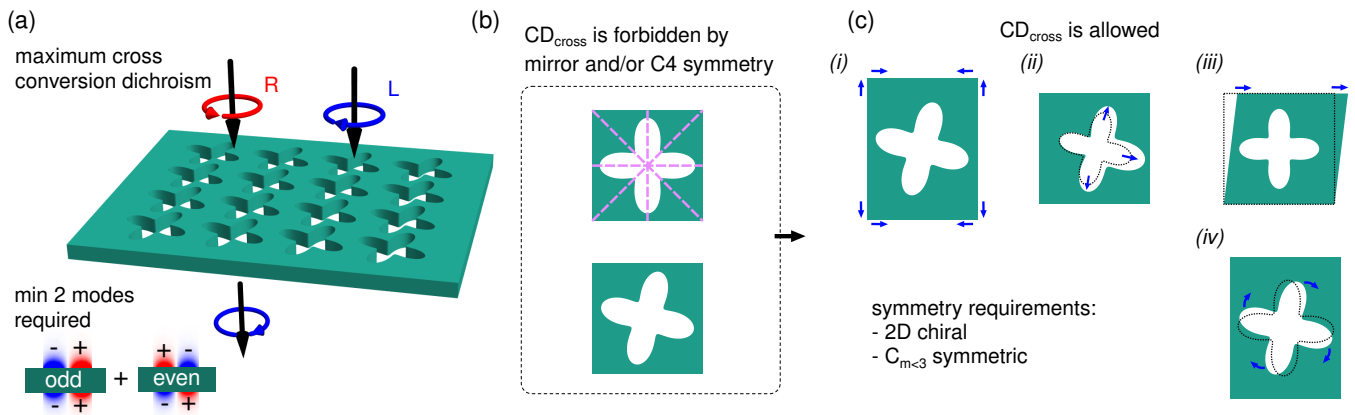


FIG. 1. **Cross conversion induced by in-plane symmetry breaking.** (a) A single-layer dielectric membrane metasurface composed of a rectangular lattice of rotated C_4 -symmetric holes supports resonantly enhanced polarization conversion. Two conditions have to be satisfied to enable the cross conversion: (1) break all in-plane mirror symmetries and (2) have $C_{m<3}$ rotationally symmetric structure. (b–c) Examples of symmetry-reduced unit cells are shown. Panels (i)–(iv) illustrate how lattice or meta-atom deformations transform the structure into a two-dimensionally chiral (2D-chiral, $C_{m<3}$ -symmetric) system where CD_{cross} becomes allowed.

Despite the practical relevance and a number of works studying particular designs, a systematic theoretical analysis of the resonant conversion circular dichroism in dielectric metasurfaces has been largely overlooked, and this is the focus of the present work. From the symmetry point of view, a nonzero CD_{cross} (2) at normal incidence requires two conditions to be simultaneously satisfied (Fig. 1):

- (i) the combined rotation-symmetry order of the meta-atom and lattice must be low enough, $m < 3$;
- (ii) the structure must lack in-plane mirror symmetry.

The first condition follows from the rotational invariance of the metasurface S-matrix, which forces all cross-polarized transmission coefficients to vanish for $m \geq 3$ (consequence of Hermann’s theorem [34]). The second condition ensures that left- and right-circular channels are not related by a mirror transformation. We discuss both in more detail in Section II.

To systematically analyze the origin of CD_{cross} , we start with C_4 rotation-symmetric single-layer membrane-metasurfaces for which it is forbidden by both conditions. Applying various in-plane perturbations we simultaneously break the in-plane mirror symmetry and the rotation symmetry and unlock resonantly enhanced CD_{cross} . As the optical properties of dielectric metasurfaces are largely determined by their resonances underpinned by excitation and emission of certain photonic eigenmodes, we analyze the underlying modal band structure and show how the observable CD_{cross} can be reduced to eigenmode interference and intercoupling described in terms of a coupled-mode theory (CMT). As we demonstrate in Sections III, one can impose a third more specific condition:

- (iii) for polarization-isotropic non-resonant background, at least two resonances must spectrally overlap.

Unlike the first two, it emerges from the structure of the resonant coupling: for a membrane with polarization-isotropic

background scattering, no spectrally isolated resonance can produce cross conversion at normal incidence, hence the co-operation of at least two overlapping modes is always required. To the best of our knowledge, this requirement has not been explicitly identified in prior works, although it has in fact always been implicitly satisfied [29, 31]. We also show that, depending on whether the interacting modes have opposite or equal parity, two distinct physical mechanisms of cross conversion arise. As a test platform we use a C_4 -symmetric membrane and progressively reduce its symmetry, observing the emergence of nonzero cross conversion (Fig. 1).

We note that the above constraints significantly differ if light is obliquely incident on a metasurface, and in particular, a spectral overlap of multiple eigenmodes is not required [35–38]. This, is beyond the scope of the present work as well as cases involving birefringent and/or optically active materials which determine trivial anisotropic nonresonant polarization conversion.

II. SYMMETRY SELECTION RULES FOR CONVERSION CIRCULAR DICHROISM

In this section we address conditions (i) and (ii). Throughout, we work with the monochromatic fields with oscillation frequency ω and adopt the $e^{-i\omega t}$ time convention, so that a decaying resonance has a negative imaginary part. In the absence of diffraction, the transmission-reflection problem is described compactly by the scattering matrix in the circular polarization basis

$$\hat{\mathbf{e}}_{\pm} = \frac{\hat{\mathbf{e}}_x \pm i \hat{\mathbf{e}}_y}{\sqrt{2}}. \quad (4)$$

Mapping between the \pm components and the right/left circular polarization (RCP/LCP) depends on the propagation direction. For a wave travelling along $+z$, $\hat{\mathbf{e}}_-$ ($\hat{\mathbf{e}}_+$) corre-

sponds to RCP (LCP), whereas for $-z$ propagation the assignment is reversed. We denote incident and outgoing channel amplitudes by $\mathbf{a} = (a_R, a_L, a'_R, a'_L)^T = (a_-, a_+, a'_+, a'_-)^T$ and $\mathbf{b} = (b_R, b_L, b'_R, b'_L)^T = (b_+, b_-, b'_-, b'_+)^T$, with primes marking the back ($z < 0$) side of the metasurface. The scattering matrix $\mathbf{b} = \mathbf{S} \cdot \mathbf{a}$ then reads [8, 25, 39]

$$\mathbf{S} = \begin{pmatrix} r_{RR} & r_{RL} & t'_{RR} & t'_{RL} \\ r_{LR} & r_{LL} & t'_{LR} & t'_{LL} \\ t_{RR} & t_{RL} & r'_{RR} & r'_{RL} \\ t_{LR} & t_{LL} & r'_{LR} & r'_{LL} \end{pmatrix}, \quad (5)$$

where second index indicate polarization of incident wave and first index indicate polarization after interacting from metasurface wave. Lorentz reciprocity requires [39]

$$\begin{aligned} t_{RR} &= t'_{RR}, & t_{LL} &= t'_{LL}, & t_{RL} &= t'_{LR}, \\ t'_{RL} &= t_{LR}, & r_{RL} &= r_{LR}, & r'_{RL} &= r'_{LR}, \end{aligned} \quad (6)$$

while the up-down mirror symmetry σ_z of a single-layer membrane additionally forces $t_{RR} = t_{LL}$. Together, these reduce the S-matrix to six independent complex parameters. The equality $t_{RR} = t_{LL}$ forces $\text{CD}_{\text{co}} = 0$ (1), while t_{RL} and t_{LR} remain independent, so any chiral response of a membrane must originate from the cross-polarized channel (2).

For a two-dimensional periodic structure, the allowed rotational symmetry orders are $m = 1, 2, 3, 4, 6$. Rotational order $m \geq 3$ forces cross-polarized transmission to zero, $t_{LR} = t_{RL} = 0$, and likewise forbids helicity-preserving reflection, $r_{RR} = r_{LL} = 0$ [25, 39]. Any in-plane mirror symmetry independently suppresses cross-conversion as well. Hence, to support CD_{cross} , a membrane metasurface must belong to the C_1 or C_2 point group with all in-plane mirrors broken.

Importantly, these conditions are necessary but not sufficient. Even in a C_1 - or C_2 -symmetric membrane with all mirror symmetries broken, a single spectrally isolated resonance cannot produce CD_{cross} . The up-down mirror symmetry of a flat membrane constrains the mode coupling coefficients in a way that for a spectrally isolated resonance cross-conversion dichroism is not possible. The interplay of at least two resonant modes is always required, as we show in the next section.

III. CHIRAL COUPLED-MODE THEORY FOR FLAT MEMBRANES

To understand why condition (iii) is necessary and to identify the physical mechanisms of cross conversion, we employ temporal coupled-mode theory (CMT).

We consider periodic systems without diffraction. Hence, there are only 4 orthogonal outgoing channels (ports). We choose the basis of circular polarizations and describe each mode's coupling to the radiative channels by a vector of coupling parameters $\mathbf{m}_n = (m_{nR}, m_{nL}, m'_{nR}, m'_{nL})^T$, where the indexes R, L denote the particular circular polarization and the primes distinguish the back ($z < 0$) metasurface side [8, 14, 22, 23]. The full $4 \times N$ coupling matrix of all considered states is built as $\mathbf{M} = (\mathbf{m}_1, \dots, \mathbf{m}_N)$.

The temporal evolution of the slow-varying mode amplitudes $\mathbf{p} = (p_1, \dots, p_N)^T$, driven by monochromatic excitation at frequency ω , is governed by [25, 40]

$$\frac{d\mathbf{p}}{dt} = i(\omega\mathbf{I} - \mathbf{\Omega} + i\mathbf{\Gamma})\mathbf{p} + \mathbf{M}^T \mathbf{a}, \quad (7)$$

where \mathbf{a} is the vector of incident wave amplitudes, \mathbf{I} is an identity matrix, $\mathbf{\Omega}$ containing the resonance frequencies on its diagonal, and $\mathbf{\Gamma}$ encoding radiative decay and far-field (port-non-orthogonal) coupling via anti-diagonal components [40]:

$$\mathbf{\Omega} = \begin{pmatrix} \omega_1 & 0 & \dots & 0 \\ 0 & \omega_2 & \dots & 0 \\ \vdots & \vdots & \ddots & \vdots \\ 0 & 0 & \dots & \omega_n \end{pmatrix}, \quad \mathbf{\Gamma} = \begin{pmatrix} \gamma_1 & \gamma_{12} & \dots & \gamma_{1n} \\ \gamma_{21} & \gamma_2 & \dots & \gamma_{2n} \\ \vdots & \vdots & \ddots & \vdots \\ \gamma_{n1} & \gamma_{n2} & \dots & \gamma_n \end{pmatrix}. \quad (8)$$

When the number of modes exceeds the number of ports, some must share radiative channels, producing off-diagonal $\gamma_{n\ell}$ in (8) [40]. We term such CMT modes *port-non-orthogonal* ($\gamma_{n\ell} \neq 0$) and *port-orthogonal* ($\gamma_{n\ell} = 0$). A non-diagonal $\mathbf{\Gamma}$ implies, according to Eq. (7), that the CMT modes mix even without external excitation. Therefore, they are distinct from the true eigenmodes found by numerical solvers (quasinormal modes), which correspond to the poles of the scattering matrix or exact solutions of the eigenvalue problem.

The outgoing wave amplitudes are determined by

$$\mathbf{b} = \mathbf{M}\mathbf{p} + \mathbf{C}\mathbf{a}, \quad (9)$$

where the first term accounts for re-radiation by the resonant modes and the second describes non-resonant background scattering through the matrix \mathbf{C} . The same coupling matrix \mathbf{M} appears in both equations, as required by Lorentz reciprocity [40]. In the absence of light energy dissipation, one can further require the energy conservation and the time-reversal symmetry of CMT equations. This yields additional constraints:

$$\mathbf{C}\mathbf{M}^* = -\mathbf{M}, \quad (10)$$

$$2\mathbf{\Gamma} = \mathbf{M}^\dagger \mathbf{M}. \quad (11)$$

Identity (11) states that all decay rates are determined by the energy leaking out through the radiative ports. Therefore, $\mathbf{\Gamma}$ here is, by construction, the radiative decay matrix, $\mathbf{\Gamma} \equiv \mathbf{\Gamma}_{\text{rad}}$. We hold to this definition throughout this work. Absorption is a separate channel that decreases the energy of a mode without feeding an outgoing port. For this reason, it does not enter \mathbf{M} . In order to account for absorption, one should substitute $\mathbf{\Omega} - i\mathbf{\Gamma} \rightarrow \mathbf{\Omega} - i\mathbf{\Gamma} - i\mathbf{\Gamma}_{\text{abs}}$ into Eq. (7) and into the S-matrix (12) below, where $\mathbf{\Gamma}_{\text{abs}}$ is a real valued diagonal matrix of absorption decay rates. The constraints (10) and (11) hold true only for $\mathbf{\Gamma}_{\text{rad}}$.

For monochromatic steady-state excitation ($d\mathbf{p}/dt = 0$), eliminating \mathbf{p} from Eqs. (7) and (9) yields the scattering matrix (see Appendix A):

$$\mathbf{S} = \mathbf{C} + i\mathbf{M}(\omega\mathbf{I} - \mathbf{\Omega} + i\mathbf{\Gamma})^{-1}\mathbf{M}^T. \quad (12)$$

TABLE I. **Bare and dressed modes summary.** The CMT coordinates of Eq. (7) and the S-matrix poles of Eq. (12) are two different objects in principle. Bare modes are the natural variables of CMT theory, while dressed modes are what numerical eigensolvers and experiments actually see. The two coincide only when Γ is diagonal. The last row assumes no losses; with losses, same-parity modes also contribute (Appendix C).

| | Bare modes | Dressed (quasinormal) modes |
|----------------------------------|-------------------------------|---|
| Definition | Enter CMT, Eq. (7) | S-matrix poles, Eq. (12) |
| How to access | Fit CMT to data | Numerical eigensolver |
| Coupling matrix | \mathbf{M} obeys (10), (11) | $\tilde{\mathbf{M}}$ may not obey (10), (11) |
| Far-field polarization | Linear, Eq. (16) | Elliptical |
| Mirror parity | | Well-defined |
| Coincide when | | Port-orthogonal limit ($\gamma_{n\ell} = 0, n \neq \ell$) |
| ΔT_{cross} origin | | Interference of opposite-parity modes |

We use two terms throughout this work. *Bare modes* are the CMT mode coordinates of (7). *Dressed modes* are those underpinning the resonances actually observed in the scattering problem. Each pole of the S-matrix (12) is one dressed mode. One can see that for the case of diagonal $\Omega - i\Gamma$ bare modes and dressed modes coincide with each other. While for a pair of interacting modes, it is possible to link bare and dressed modes, in a general case this connection is rather unknown. This distinction, though rarely emphasized, is noted in Ref. [40]. To the best of our knowledge, a rigorous link between quasi-normal modes and bare CMT modes in the general case remains an open challenge.

Generally, the background non-resonant scattering matrix \mathbf{C} can have both isotropic and anisotropic contributions. The anisotropic part may produce conversion similar to a birefringent wave-plate. However, such contributions are typically low for thin dielectric membranes, hence we assume the background to be isotropic:

$$\mathbf{C} \approx \begin{pmatrix} 0 & \rho & \tau & 0 \\ \rho & 0 & 0 & \tau \\ \tau & 0 & 0 & \rho \\ 0 & \tau & \rho & 0 \end{pmatrix}. \quad (13)$$

In the absence of background dissipation, this matrix is unitary, $\mathbf{C}^\dagger \mathbf{C} = \mathbf{1}$, which determines that $|\rho|^2 + |\tau|^2 = 1$ and $\arg(\rho) = \arg(\tau) \pm \frac{\pi}{2}$. It is convenient to parametrize it using two real parameters

$$\tau = e^{i\alpha} \cos \beta, \quad \rho = ie^{i\alpha} \sin \beta. \quad (14)$$

where the phase $\alpha \in [0, 2\pi]$, and the merit of background transparency $\beta \in [-\pi/2, \pi/2]$.

We now focus on further simplifications of CMT parameters related to the membrane-metasurface symmetry. The out-of-plane mirror symmetry of a flat membrane assigns a definite parity p_n to each mode: even ($p_n = +1$) and odd ($p_n = -1$). This constrains the coupling parameters on opposite sides of the membrane as [23]:

$$m'_{nR} = p_n m_{nL}, \quad m'_{nL} = p_n m_{nR}. \quad (15)$$

Combined with the time-reversal constraint (10) and the isotropic background (13), this yields (Appendix A)

$$|m_{nR}| = |m_{nL}|, \quad (16)$$

for every bare mode irrespective of its parity: each couples equally to LCP and RCP waves, so its far field is *linearly polarized*. A single resonance therefore cannot generate CD_{cross} and at least two bare modes must cooperate. Note that Eq. (16) holds true only for bare modes. As we show below, when bare modes overlap in frequency, the off-diagonal entries in Γ can hybridize them into *dressed eigenmodes* whose far fields may turn elliptical and provide mode-level chirality. The essential differences between bare and dressed modes are collected in Tab. I.

From the energy conservation requirement (11) it follows, regardless of the mode parity, that $\gamma_n = 2|m_{nR}|^2 = 2|m_{nL}|^2$. Combining this with the parametrization as in Eq. (14) and the time-reversal constraint (10), we can express the coupling parameters in the following form (Appendix A):

$$\begin{aligned} m_{nR} &= i^{(1+p_n)/2} \sqrt{\frac{\gamma_n}{2}} \exp\left(i \frac{\alpha + p_n \beta}{2} - i\theta_n\right), \\ m_{nL} &= i^{(1+p_n)/2} \sqrt{\frac{\gamma_n}{2}} \exp\left(i \frac{\alpha + p_n \beta}{2} + i\theta_n\right). \end{aligned} \quad (17)$$

Here the prefactor $i^{(1+p_n)/2}$ is equal to i for $p_n = 1$ and to 1 for $p_n = -1$. Physically, the angle θ_n characterizes the direction of the far-field linear polarization of a CMT mode with respect to the x -axis.

The mechanisms by which two or more modes produce nonzero CD_{cross} depend on whether the interacting modes are *port-orthogonal*. We call two modes n and ℓ port-orthogonal when

$$\mathbf{m}_n^\dagger \mathbf{m}_\ell = 0. \quad (18)$$

Non-orthogonal modes coherently drive one another through the shared radiative channels, establishing an indirect coupling mediated by the radiation continuum [40]. By virtue of energy conservation $2\Gamma = \mathbf{M}^\dagger \mathbf{M}$, the port-orthogonality (18) is equivalent to $\gamma_{n\ell} = 0$ with $n \neq \ell$: port-orthogonal modes radiate into non-overlapping far-field patterns and evolve independently, each contributing an independent Lorentzian to the S-matrix.

This leads to two distinct mechanisms of cross conversion:

- (A) *Port-orthogonal mechanism.* Modes of opposite parity are always port-orthogonal, and the matrix $\Omega - i\Gamma$ is di-

agonal. The S-matrix (12) decomposes into a sum of independent Lorentzian contributions. Cross conversion dichroism arises from the interference of these contributions.

- (B) *Port-non-orthogonal mechanism.* Same-parity modes with non-orthogonal far fields hybridize through their shared radiation channels, and the dressed modes can become elliptically polarized. While alone they give $\Delta T_{\text{cross}} = 0$, a nonzero conversion dichroism needs an extra opposite-parity mode or material losses.

We illustrate each mechanism with a minimal model and full-wave numerics.

A. Port-orthogonal mechanism: opposite-parity modes

Opposite-parity modes ($p_1 = -p_2$) automatically satisfy the port-orthogonality condition (18) via the parity relations (15), regardless of the polarization angles θ_n . The dissipation matrix is therefore diagonal,

$$\mathbf{\Omega} - i\mathbf{\Gamma} = \begin{pmatrix} \Omega_1 & 0 \\ 0 & \Omega_2 \end{pmatrix}, \quad \Omega_n = \omega_n - i\gamma_n, \quad (19)$$

bare and dressed modes coincide, and the S-matrix (12) reduces to a sum of independent Lorentzians

$$\mathbf{S} = \mathbf{C} - \sum_n \frac{\mathbf{m}_n \mathbf{m}_n^T}{i(\omega - \omega_n) - \gamma_n}. \quad (20)$$

Substituting the parametrization (17) gives the cross-polarized amplitudes in closed form:

$$t_{\text{LR}} = \sum_n A_n e^{-2i\theta_n}, \quad t_{\text{RL}} = \sum_n A_n e^{+2i\theta_n}, \quad (21)$$

$$A_n = \frac{(\gamma_n/2) e^{i(\alpha + p_n \beta)}}{i(\omega - \omega_n) - \gamma_n}.$$

For a single resonance $|t_{\text{LR}}^{(n)}| = |t_{\text{RL}}^{(n)}|$, consistent with Eq. (16). Cross-conversion dichroism therefore arises only from interference between the two Lorentzians. Denoting the polarization-angle difference $\Delta\theta = \theta_1 - \theta_2$, the chiral signal carries a universal angular factor,

$$|t_{\text{LR}}|^2 - |t_{\text{RL}}|^2 = 4 \sin(2\Delta\theta) \text{Im}(A_1 A_2^*). \quad (22)$$

Opposite parity puts the two background phases $e^{i(\alpha + p_n \beta)}$ on opposite branches, so $A_1 A_2^*$ carries a relative factor $e^{-2ip_1 \beta}$, which makes $\text{Im}(A_1 A_2^*) \neq 0$ in general. The cross-conversion dichroism is therefore nonzero whenever $\sin 2\Delta\theta \neq 0$ and the modes are spectrally non-degenerate. Chirality is encoded in the relative complex phase between two linearly polarized bare resonances of opposite parity, not at the level of any single eigenmode.

Now we analyze the main result (22) for the two port-orthogonal modes. The maximum values of (22) is achieved for 50% background transmission ($\beta = \pi/4$), 45 degree angle

between far field linear polarizations, $\Delta\theta = \pm\pi/4$, and equal real frequencies $\omega_1 = \omega_2$. As soon as decay rates are different $\gamma_1 \neq \gamma_2$, one should observe antisymmetric flip. We illustrate different regimes in Fig. 4.

We now illustrate the theory with a numerical example shown in Fig. 2. We start our design with a freestanding membrane metasurface with the high of H and made of lossless dielectric with relative permittivity ϵ . The membrane has a period perforation with the period P_x (P_y) along the x -axis (y -axis) of a four-pedal holes defined by a parametric equation

$$r(\phi) = r_0 + r_1 \cos[4(\phi + \theta)]. \quad (23)$$

By fixing $P_x = P_y$, we start with a C_4 symmetric design which despite being 2D chiral forbids any cross conversion as was derived in Sec. II. All modes with can radiate into the continuum in this system are double degenerate (this is a consequence of C_n symmetry for all systems with $n \geq 3$), see more in Refs. [22, 23, 41–43]. Next, we do the area preserving squeezing of the unit cell by keeping $P_x P_y = \text{const}$ [see Fig. 2(b)]. This operation reduces rotational symmetry from four fold to a two fold. Degeneracy of the modes is lifted and we observe a splitting in their positions [shown by color in Fig. 2(b)]. The colored lines shows the far field polarization of the eigen modes. Since we do not break up-down mirror symmetry, the parity is preserved. Around 1635 nm and $P_y/P_x = 1.12$ modes of different parities cross. Since these modes are port-orthogonal, and they are spectrally isolated from any other modes, their far polarization is linear and can be described by an angle θ_n with the x -axis. This is in the agreement with Eq. (16). The numerical values exactracted from the eigen value solver of COMSOL are $\Omega_1 \approx 1150 - i20$ THz, $\Omega_2 \approx 1152 - i8$ THz, $\theta_1 \approx -0.39$, $\theta_2 \approx 0.14$, $p_1 = +1$, and $p_2 = -1$ [field profiles in Fig. 2(a)]. Since bare modes for port-orthogonal crossing coincide with the true dressed modes, we are left with only two free parameters in Eqs. (21)–(22): the background parameters α and β introduced in Eq. (14). By varying only these two parameters we are able to achieve good agreement between full numerical transmission calculations and the two mode model at $\alpha_{\text{fit}} = -146^\circ$ and $\beta_{\text{fit}} = -63^\circ$ [see Fig. 2(c,d)]. Scanning ΔT_{cross} over the full $(P_y/P_x, \lambda)$ plane [Fig. 2(b)] confirms that the conversion dichroism (3) peaks precisely at the opposite-parity crossing, as predicted by the master equation (22) which is extrenal at $\omega_1 = \omega_2$.

B. Port-non-orthogonal mechanism: same-parity modes

Now we turn into the analyses of the port-non-orthogonal mechanism of the modes with close frequencies. In the current CMT model, we always have $\Delta T_{\text{cross}} = 0$ for 2 and more modes of the same parity spectrally isolated from modes of an opposite parity. Either a mode of opposite parity or a present of material losses are always required (Appendix C).

For that purpose we consider a three mode model with a non-diagonal elements in the $\mathbf{\Gamma}$ matrix. In that case bare CMT

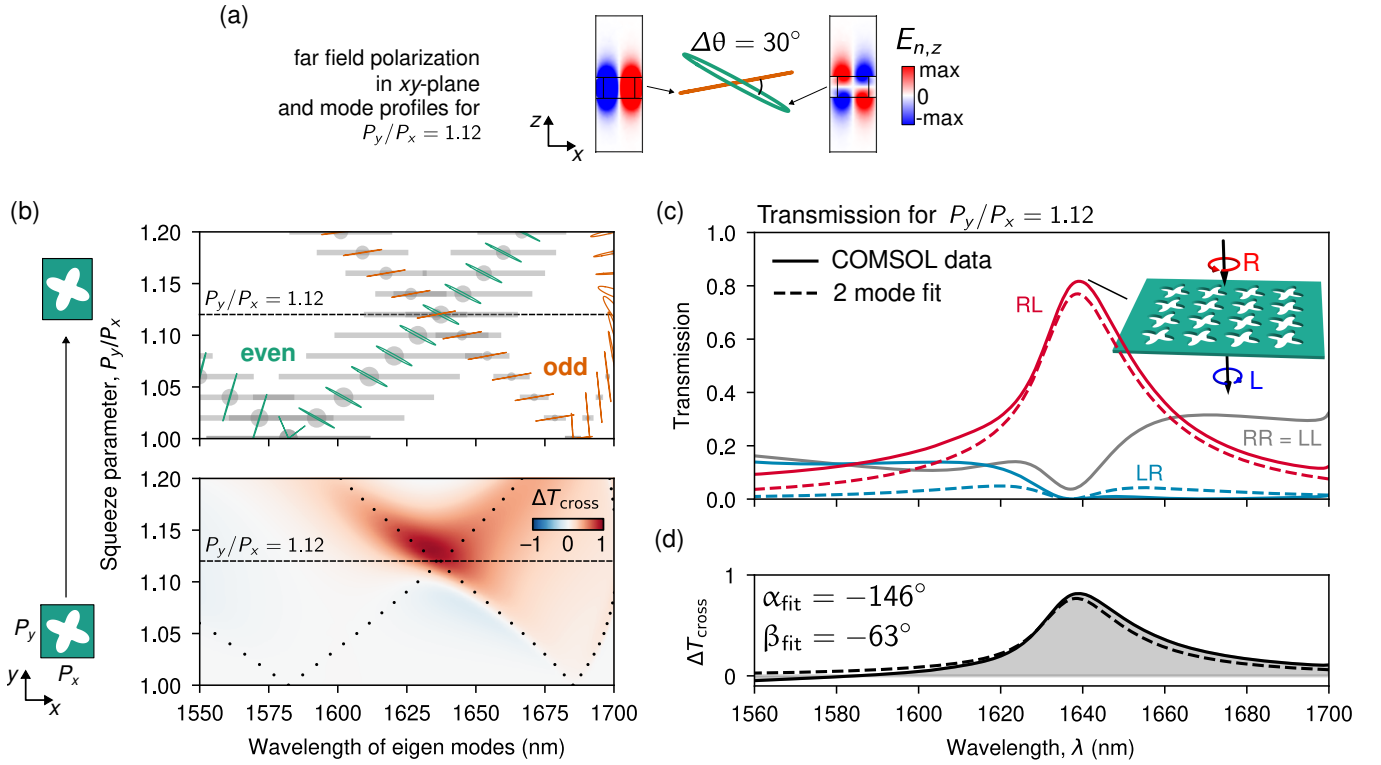


FIG. 2. **Port-orthogonal mechanism: opposite-parity modes.** (a) $E_{n,z}$ field profiles of the two modes at the crossing, illustrating their opposite up-down mirror parities. (b, top) Eigenmode wavelengths under area-preserving squeezing of the unit cell ($P_x P_y = \text{const}$), reducing the symmetry from C_4 to C_2 . The C_4 double degeneracy splits into two branches; color encodes the parity $p_n = \pm 1$ ($^{\text{even}}$ / $^{\text{odd}}$), the colored lines show the far-field polarization, and gray bars mark the linewidth $\Delta\lambda_n = \lambda_n/Q_n$. Opposite-parity modes cross near $\lambda \approx 1635$ nm at $P_y/P_x \approx 1.12$. (b, bottom) Map of ΔT_{cross} in the $(P_y/P_x, \lambda)$ plane from full-wave numerics: the conversion dichroism peaks at the opposite-parity crossing, in agreement with the master equation (22) which predicts the maximum performac at $\omega_1 = \omega_2$. (c,d) Co- and cross-polarized transmission (c) and cross-conversion dichroism ΔT_{cross} (d) taken at $P_y/P_x = 1.12$: full-wave numerics versus the two-mode model (21)–(22), with only the background parameters fitted, $\alpha_{\text{fit}} = -146^\circ$, $\beta_{\text{fit}} = -63^\circ$. Simulation parameters: membrane height $H = 400$ nm, period $P_x = 1$ μm , hole contour from Eq. (23) with $r_0 = 300$ nm, $r_1 = 123$ nm, and $\theta = \pi/8$.

modes do not coincide with the true eigen modes of the system and diagonalization procedure must be done. In general, analytics becomes cumbersome and heavy to analyse, yet we still present a convenient parametrization approach. Substituting the parametrization (17) together with the parity relations (15) into the port-orthogonality condition (18) gives, for two same-parity modes ($p_1 = p_2$),

$$\mathbf{m}_1^\dagger \mathbf{m}_2 = 2\sqrt{\gamma_1 \gamma_2} \cos(\Delta\theta_{12}), \quad \Delta\theta_{12} = \theta_1 - \theta_2, \quad (24)$$

and $\mathbf{m}_1^\dagger \mathbf{m}_2 = 0$ for opposite parity ($p_1 = -p_2$). Same-parity modes are therefore port-orthogonal iff their far-field polarizations are perpendicular [$\cos(\Delta\theta_{12}) = 0$]. However, generally $\cos \Delta\theta \neq 0$ and the modes are port-non-orthogonal. Energy conservation $2\Gamma = \mathbf{M}^\dagger \mathbf{M}$ then identifies the off-diagonal decay rate as $\gamma_{12} = \sqrt{\gamma_1 \gamma_2} \cos(\Delta\theta_{12})$. We can generalize it for 3 mode case as

$$\gamma_{ij} = \frac{1 + p_i p_j}{2} \sqrt{\gamma_i \gamma_j} \cos(\Delta\theta_{ij}), \quad (25)$$

and the CMT matrix $\Omega - i\Gamma$ (8) acquires off-diagonal elements.

Using general equation for the scattering matrix (12) and parametrization (17) we construct a fitting model based on several meaningful parameters: two parameters to define amplitude and phase of the transmission, e.g. angles $\alpha \in [0, 2\pi]$ and $\beta \in [-\pi/2, \pi/2]$; and three parameters for each bare mode, namely its resonant position ω_n , spectral linewidth γ_n , and its far field polarization angle θ_n . Once it is done, the complex orthogonal diagonalization matrix \mathbf{T} ($\mathbf{T}^T \mathbf{T} = \mathbf{1}$) can be found numerically which gives the frequency of the dressed modes $\tilde{\Omega}_n$:

$$\mathbf{T}^T (\Omega - i\Gamma) \mathbf{T} = \begin{pmatrix} \tilde{\Omega}_1 & 0 & 0 \\ 0 & \tilde{\Omega}_2 & 0 \\ 0 & 0 & \tilde{\Omega}_3 \end{pmatrix}, \quad (26)$$

and the corresponding dressed coupling parameters

$$\tilde{\mathbf{M}} = \mathbf{M} \mathbf{T}. \quad (27)$$

Time reversal constraint (10) and energy conservation identity (11) are no longer satisfied for the dressed parameters $\tilde{\mathbf{M}}$ defined by the transformation \mathbf{T} in Eq. (27). Hence, conclusion about linear polarization (16) is no longer applicable to

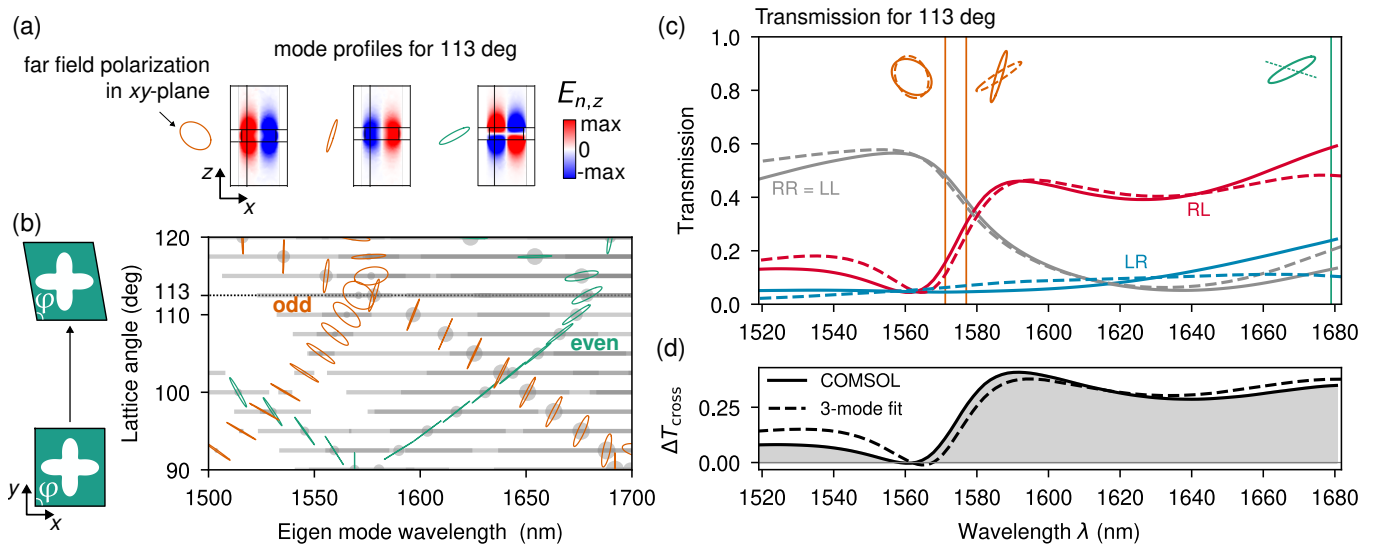


FIG. 3. **Port-non-orthogonal mechanism: same-parity modes.** (a) $E_{n,z}$ field profiles of the three involved modes at the crossing, illustrating their up-down mirror parities. (b) Eigenmode wavelengths versus the lattice angle φ , deforming a rectangular lattice ($\varphi = 90^\circ$) into a 2D-chiral monoclinic one. Color encodes the parity $p_n = \pm 1$ ($^{\text{even}}$ / $^{\text{odd}}$), ellipses show the far-field polarization, and gray bars mark the linewidth $\Delta\lambda_n = \lambda_n/Q_n$. Near $\varphi \approx 113^\circ$ two same-parity modes cross; port-non-orthogonal mixing turns one dressed mode circularly polarized, violating the bare-mode result (16). (c,d) Co- and cross-polarized transmission (c) and cross-conversion dichroism ΔT_{cross} (3) (d): full-wave numerics versus the three-mode model (12), fitted with the parameters listed in Tab. II. Simulation parameters: $\varepsilon = 12$, height $H = 300$ nm, hole contour from Eq. (23) with $r_0 = 300$ nm, $r_1 = 123$ nm, $\theta = 0$; periods $P_x = 1$ μm , $P_y = 1.05$ μm .

TABLE II. **Three mode model fitting parameters.** Mode complex frequencies (in 2π THz) from COMSOL eigenmode simulation (conjugated to $e^{-i\omega t}$ convention), dressed modes as the result of diagonalization (26), and the fitting parameters: the bare CMT modes complex frequencies Ω_n and their polarization angles θ_n ; and background angles: $\alpha = 13.8^\circ$, $\beta = -55.3^\circ$.

| p_n | Ω_n^{COMSOL} | $\tilde{\Omega}_n$ (dressed) | Ω_n (fit) | θ_n (fit) |
|-------|----------------------------|------------------------------|------------------|------------------|
| +1 | 1121.9 - i36.2 | 1121.9 - i36.1 | 1121.9 - i36.1 | 16.9 $^\circ$ |
| -1 | 1194.4 - i41.5 | 1194.4 - i41.5 | 1185.6 - i29.8 | 166.8 $^\circ$ |
| -1 | 1198.8 - i12.1 | 1198.9 - i12.1 | 1207.7 - i23.9 | 119.3 $^\circ$ |

the dressed modes, and *elliptically polarized modes are allowed*. Finally, once the S -matrix is calculated numerically via Eq. (12), the cross conversion dichroism can be calculated directly using its connection with the transmission coefficients, Eq. (5).

Let us demonstrate a vivid example of such 3 mode mixing, which produce circularly polarized in the far field modes. We start with a free standing membrane made of dielectric with $\varepsilon = 12$ and height $H = 300$ nm. It has perforation of four-fold holes define by a parametric equation (23) with $r_0 = 300$ nm, $r_1 = 123$ nm, and $\theta = 0$. The holes form a rectangular arrangement with the periods $P_x = 1$ μm and $P_y = 1.05$ μm . Since the four-fold cut is aligned with the periodic arrangement, there is no 2D chirality yet [12]. Next, we deform the lattice angle φ from 90° to larger values, while keeping other parameters constant [Fig. 3(b)]. In doing so, we transition from rectangular lattice to a 2D chiral monoclinic arrangement, which lacks all possible in-plane mirror

symmetric [12, 14, 44, 45].

In Fig. 3(b) we show the eigen mode evolution depending on the lattice angle, where color shows the up-down mirror parity (illustrated by the field profiles in panel (a)) and small ellipses show the far field polarization. Gray horizontal bars show spectral linewidth defined as $\Delta\lambda_n = \lambda_n/Q_n$. Around $\varphi = 113^\circ$ we observe a crossing of the same parity modes. One of the modes is circularly polarized. This is the consequence of the port-non-orthogonal mixing, which violates the result (16) obtained for the bare modes, as numerical eigen value solver provides rather dressed modes. This crossing is not spectrally isolated and in its vicinity there a third mode of opposite parity. Hence, to describe the cross conversion dichroism in this case we have to employ the three mode model developed in this section.

We calculate the transmission and conversion dichroism using full numerical model [Fig. 3(c,d)]. Next, we use a numerical fit of the three mode model. The fitting parameters are modes bare frequencies Ω_n and polarization angles θ_n , as well as the background angles α and β from (14). We set the target of the minimization procedure to be the minimal difference in the co- and cross-polarized transmissions, as well as the closeness of the dressed frequencies to the ones obtained by a numerical solver. We show the final values in the Tab. II, and observe a good agreement between the full numerical model and a three mode CMT model.

IV. CONCLUSION

We have analyzed, both numerically and theoretically, the manifestation of chiral properties of single-layer dielectric structured membrane metasurfaces. We have assumed that the metasurface is vertically symmetric, but it has a broken in-plane symmetry introduced by deformations of the unit cell. In a sharp contrast to a common belief that chiral optical phenomena require symmetry breaking in the vertical direction, we have revealed that single-layer metasurfaces can demonstrate strong resonant chiral effects. As a matter of fact, strong circular dichroism appears as a cross-polarization conversion due to resonances of photonic eigenmodes in a finite-width metasurface. We have explored this effect for a specific exam-

ple of a C_4 rotation-symmetric metasurface with in-plane perturbations. Breaking the in-plane mirror symmetry and lifting the rotation symmetry unlocks circular conversion dichroism near resonances. We have established general selection rules for this effect and have traced its connection with the eigenmode interference and inter-coupling by employing the chiral coupled-mode theory.

ACKNOWLEDGMENTS

B.K. acknowledges a support of Prime Minister Research Fellowship from Ministry of Science and Technology, India. Y.K. thanks Dr. Peng Xie for his initial participation in a related project. The collaborative work on this project began in 2025.

-
- [1] William Thomson Kelvin. *The molecular tactics of a crystal*. Clarendon Press, 1894.
- [2] Augustin-Jean Fresnel. Considérations théoriques sur la polarisation de la lumière. *Bull. Sci. Soc. Philomath*, pages 147–158, 1824.
- [3] Laurence D. Barron. From Cosmic Chirality to Protein Structure: Lord Kelvin’s Legacy. *Chirality*, 24(11):879–893, November 2012.
- [4] Prasad L. Polavarapu, editor. *Chiral analysis: advances in spectroscopy, chromatography and emerging methods*. Elsevier, Amsterdam, second edition edition, 2018.
- [5] C Bustamante, I Tinoco, and M F Maestre. Circular differential scattering can be an important part of the circular dichroism of macromolecules. *Proceedings of the National Academy of Sciences*, 80(12):3568–3572, June 1983.
- [6] Jagadis Chunder Bose. On the Rotation of Plane of Polarisation of Electric Waves by a Twisted Structure. *Proceedings of the Royal Society of London*, 6:146–152, 1898.
- [7] Karl F. Lindman. Über eine durch ein isotropes System von spiralförmigen Resonatoren erzeugte Rotationspolarisation der elektromagnetischen Wellen. *Annalen der Physik*, 368(23):621–644, 1920.
- [8] Maxim V. Gorkunov, Alexander A. Antonov, and Yuri S. Kivshar. Metasurfaces with Maximum Chirality Empowered by Bound States in the Continuum. *Phys. Rev. Lett.*, 125(9):093903, 2020.
- [9] Xudong Zhang, Yilin Liu, Jiecai Han, Yuri Kivshar, and Qinghai Song. Chiral emission from resonant metasurfaces. *Science*, 377(6611):1215–1218, September 2022.
- [10] Yang Chen, Huachun Deng, Xinbo Sha, Weijin Chen, Ruize Wang, Yu-Hang Chen, Dong Wu, Jiaru Chu, Yuri S. Kivshar, Shumin Xiao, and Cheng-Wei Qiu. Observation of intrinsic chiral bound states in the continuum. *Nature*, 613(7944):474–478, January 2023.
- [11] Kirill Koshelev, Yutao Tang, Zixian Hu, Ivan I. Kravchenko, Guixin Li, and Yuri Kivshar. Resonant Chiral Effects in Nonlinear Dielectric Metasurfaces. *ACS Photonics*, 10(1):298–306, 2023.
- [12] Ivan Sinev, Felix Ulrich Richter, Ivan Toftul, Nikita Glebov, Kirill Koshelev, Yongsop Hwang, David G. Lancaster, Yuri Kivshar, and Hatice Altug. Chirality encoding in resonant metasurfaces governed by lattice symmetries. *Nat. Commun.*, 16(6091):6091, 2025.
- [13] Dmytro Gryb, Fedja J. Wendisch, Andreas Aigner, Thorsten Götz, Andreas Tittl, Leonardo de S. Menezes, and Stefan A. Maier. Two-Dimensional Chiral Metasurfaces Obtained by Geometrically Simple Meta-atom Rotations. *Nano Lett.*, 23(19):8891–8897, 2023.
- [14] Ivan Toftul, Pavel Tonkaev, Kirill Koshelev, Fangxing Lai, Qinghai Song, Maxim Gorkunov, and Yuri Kivshar. Chiral Dichroism in Resonant Metasurfaces with Monoclinic Lattices. *Phys. Rev. Lett.*, 133(21):216901, 2024.
- [15] Bo Wang, Tingyue Zhu, Yunan Liu, Haifang Yang, Ruhao Pan, and Junjie Li. Chiral Resonant Modes Induced by Intrinsic Birefringence in Lithium Niobate Metasurfaces. *Phys. Rev. Lett.*, 134(11):113802, 2025.
- [16] Youwen An, Wei Zhang, Tianjiao Du, Mingxuan Liu, Zuolong Li, Quan Xu, Xueqian Zhang, Liyuan Liu, Chunmei Ouyang, Jianqiang Gu, and Dan Luo. Soft-MEMS Chiral Reconfigurable Terahertz Metasurfaces Based on Liquid Crystal Elastomer. *Adv. Funct. Mater.*, n/a(n/a):e75428, 2026.
- [17] Lucca Kühner, Fedja J. Wendisch, Alexander A. Antonov, Johannes Bürger, Ludwig Hüttenhofer, Leonardo de S. Menezes, Stefan A. Maier, Maxim V. Gorkunov, Yuri Kivshar, and Andreas Tittl. Unlocking the out-of-plane dimension for photonic bound states in the continuum to achieve maximum optical chirality. *Light Sci. Appl.*, 12(250):250, 2023.
- [18] Maxim V. Gorkunov, Alexander A. Antonov, Vladimir R. Tuz, Anton S. Kupriianov, and Yuri S. Kivshar. Bound States in the Continuum Underpin Near-Lossless Maximum Chirality in Dielectric Metasurfaces. *Adv. Opt. Mater.*, 9(19):2100797, 2021.
- [19] Connor Heimig, Alexander A. Antonov, Dmytro Gryb, Thomas Possmayer, Thomas Weber, Michael Hirler, Jonas Biechteler, Luca Sortino, Leonardo de S. Menezes, Stefan A. Maier, Maxim V. Gorkunov, Yuri Kivshar, and Andreas Tittl. Chiral nonlinear polaritonics with van der Waals metasurfaces. *Sci. Adv.*, 12(13), 2026.
- [20] Xudong Zhang, Yilin Liu, Jiecai Han, Yuri Kivshar, and Qinghai Song. Chiral emission from resonant metasurfaces. *Science*, 377(6611):1215–1218, 2022.
- [21] Yang Chen, Huachun Deng, Xinbo Sha, Weijin Chen, Ruize Wang, Yu-Hang Chen, Dong Wu, Jiaru Chu, Yuri S. Kivshar, Shumin Xiao, and Cheng-Wei Qiu. Observation of intrinsic chiral bound states in the continuum. *Nature*, 613:474–478,

- 2023.
- [22] Maxim V. Gorkunov, Alexander A. Antonov, Alena V. Mamonova, Egor A. Muljarov, and Yuri Kivshar. Substrate-Induced Maximum Optical Chirality of Planar Dielectric Structures. *Adv. Opt. Mater.*, 13(3):2402133, 2025.
- [23] Brijesh Kumar, Ivan Toftul, Anshuman Kumar, Maxim Gorkunov, and Yuri Kivshar. Maximal Optical Chirality via Mode Coupling in Bilayer Metasurfaces. *ACS Photonics*, 12(12):6717–6727, 2025.
- [24] Brijesh Kumar, Pavel Tonkaev, Ivan Toftul, Yihong Chen, Vaishakh Unnikrishnan, Albert Mathew, Anshuman Kumar, Furkan Kuruoglu, Filiz Yesilkoy, and Yuri Kivshar. Intrinsic chirality of dielectric metasurfaces unlocked by resonant chiral modes, May 2026. arXiv:2605.11366 [physics.optics].
- [25] Maxim V. Gorkunov and Alexander A. Antonov. *Rational design of maximum chiral dielectric metasurfaces*, pages 243–286. Elsevier, 2024.
- [26] Behrooz Semnani, Jeremy Flannery, Rubayet Al Maruf, and Michal Bajcsy. Spin-preserving chiral photonic crystal mirror. *Light: Science & Applications*, 9(1), February 2020.
- [27] Tan Shi, Zi-Lan Deng, Guangzhou Geng, Xianzhi Zeng, Yixuan Zeng, Guangwei Hu, Adam Overvig, Junjie Li, Cheng-Wei Qiu, Andrea Alù, Yuri S. Kivshar, and Xiangping Li. Planar chiral metasurfaces with maximal and tunable chiroptical response driven by bound states in the continuum. *Nature Communications*, 13(1):4111, December 2022.
- [28] Kirill Voronin, Alexey S. Taradin, Maxim V. Gorkunov, and Denis G. Baranov. Single-handedness chiral optical cavities. *ACS Photonics*, 9(8):2652–2659, May 2022.
- [29] V. A. Fedotov, P. L. Mladyonov, S. L. Prosvirnin, A. V. Rogacheva, Y. Chen, and N. I. Zheludev. Asymmetric Propagation of Electromagnetic Waves through a Planar Chiral Structure. *Phys. Rev. Lett.*, 97(16):167401, 2006.
- [30] V. A. Fedotov, A. S. Schwanecke, N. I. Zheludev, V. V. Khardikov, and S. L. Prosvirnin. Asymmetric Transmission of Light and Enantiomerically Sensitive Plasmon Resonance in Planar Chiral Nanostructures. *Nano Lett.*, 7(7):1996–1999, July 2007.
- [31] E. Plum, V. A. Fedotov, and N. I. Zheludev. Planar metamaterial with transmission and reflection that depend on the direction of incidence. *Appl. Phys. Lett.*, 94(13):131901, 2009.
- [32] Chihhui Wu, Nihal Arju, Glen Kelp, Jonathan A. Fan, Jason Dominguez, Edward Gonzales, Emanuel Tutuc, Igal Brener, and Gennady Shvets. Spectrally selective chiral silicon metasurfaces based on infrared Fano resonances. *Nat. Commun.*, 5(3892):3892, 2014.
- [33] Jingpei Hu, Xiaonan Zhao, Yu Lin, Aijiao Zhu, Xiaojun Zhu, Peiji Guo, Bing Cao, and Chinhua Wang. All-dielectric metasurface circular dichroism waveplate. *Sci. Rep.*, 7(41893):41893, January 2017.
- [34] Carl Hermann. Tensoren und Kristallsymmetrie. *Zeitschrift für Kristallographie*, 89:32–48, 1934.
- [35] Zhichun Fan, Zhichun Fan, Zhichun Fan, Liang Wang, Hengwei Shen, and Hengwei Shen. Maximum extrinsic chirality flip and spin-dependent near-field imaging induced by bound state in the continuum. *Opt. Express*, 33(13):26993–27002, 2025.
- [36] Wenzhe Liu, Bo Wang, Yiwen Zhang, Jiajun Wang, Maoxiong Zhao, Fang Guan, Xiaohan Liu, Lei Shi, and Jian Zi. Circularly Polarized States Spawning from Bound States in the Continuum. *Phys. Rev. Lett.*, 123(11):116104, 2019.
- [37] E. Plum, V. A. Fedotov, and N. I. Zheludev. Optical activity in extrinsically chiral metamaterial. *Appl. Phys. Lett.*, 93(19):191911, 2008.
- [38] E. Plum, X.-X. Liu, V. A. Fedotov, Y. Chen, D. P. Tsai, and N. I. Zheludev. Metamaterials: Optical Activity without Chirality. *Phys. Rev. Lett.*, 102(11):113902, 2009.
- [39] Kirill Koshelev, Ivan Toftul, Yongsop Hwang, and Yuri Kivshar. Scattering matrix for chiral harmonic generation and frequency mixing in nonlinear metasurfaces. *J. Opt.*, 26(5):055003, 2024.
- [40] Wonjoo Suh, Zheng Wang, and Shanhuai Fan. Temporal coupled-mode theory and the presence of non-orthogonal modes in lossless multimode cavities. *IEEE Journal of Quantum Electronics*, 40(10):1511–1518, oct 2004.
- [41] Vladimir Igoshin, Mariia Tsimokha, Anastasia Nikitina, Mihail Petrov, Ivan Toftul, and Kristina Frizyuk. Exceptional points in single open acoustic resonator due to symmetry breaking. *Phys. Rev. B*, 109(14):144102, 2024.
- [42] Adrià Canós Valero, Vjaceslavs Bobrovs, Thomas Weiss, Lei Gao, Alexander S. Shalin, and Yuri Kivshar. Bianisotropic exceptional points in an isolated dielectric nanoparticle. *Phys. Rev. Res.*, 6(1):013053, 2024.
- [43] Sergey Gladyshev, Kristina Frizyuk, and Andrey Bogdanov. Symmetry analysis and multipole classification of eigenmodes in electromagnetic resonators for engineering their optical properties. *Phys. Rev. B*, 102(7):075103, 2020.
- [44] Ivan Toftul, Dhruv Hariharan, Pavel Tonkaev, Fangxing Lai, Qinghai Song, and Yuri Kivshar. Monoclinic nonlinear metasurfaces for resonant engineering of polarization states. *Nanophotonics*, 2025.
- [45] Kaili Sun, Bingxiong Yang, Yangjian Cai, Yuri Kivshar, and Zhanghua Han. Circularly polarized thermal emission driven by chiral flatbands in monoclinic metasurfaces. *Sci. Adv.*, 11(31), 2025.

Appendix A: Coupled-mode theory of flat membranes

Setting $d\mathbf{p}/dt = 0$ in Eq. (7) gives the steady-state amplitudes $\mathbf{p} = i(\omega\mathbf{I} - \mathbf{\Omega} + i\mathbf{\Gamma})^{-1}\mathbf{M}^T\mathbf{a}$. Substituting them into Eq. (9) yields the scattering matrix (12). Throughout this appendix we abbreviate the effective non-Hermitian Hamiltonian as $\mathbf{H} \equiv \mathbf{\Omega} - i\mathbf{\Gamma}$, so that $\mathbf{S} = \mathbf{C} + i\mathbf{M}(\omega\mathbf{I} - \mathbf{H})^{-1}\mathbf{M}^T$.

1. Coupling parameters of bare modes

A flat membrane is invariant with respect to the $z \leftrightarrow -z$ interchange and its eigenstates can be categorized by their parity with respect to the z -axis. We denote even modes having even transversal and odd normal electric field components (see the derivation using group theory in the SM of Ref. [23]):

$$\begin{aligned} E_{\text{even } x,y}(x, y, z) &= E_{\text{even } x,y}(x, y, -z), \\ E_{\text{even } z}(x, y, z) &= -E_{\text{even } z}(x, y, -z), \end{aligned} \quad (\text{A1})$$

while the opposite is true for the odd modes:

$$\begin{aligned} E_{\text{odd } x,y}(x, y, z) &= -E_{\text{odd } x,y}(x, y, -z) \\ E_{\text{odd } z}(x, y, z) &= E_{\text{odd } z}(x, y, -z). \end{aligned} \quad (\text{A2})$$

For the coupling parameters, this allows relating those on the opposite metasurface sides as

$$m'_{\text{even R}} = m_{\text{even L}}, \quad m'_{\text{even L}} = m_{\text{even R}}, \quad (\text{A3})$$

for even modes, and

$$m'_{\text{odd R}} = -m_{\text{odd L}}, \quad m'_{\text{odd L}} = -m_{\text{odd R}}, \quad (\text{A4})$$

for the odd ones. In the parity notation of the main text these are $p_n = +1$ (even) and $p_n = -1$ (odd), so Eqs. (A3) and (A4) are the two cases of Eq. (15).

For adequate description of chiral effects, we have to express all polarization conversion effects by the participating modes. The background channels are then polarization independent and amount to an isotropic background S-matrix:

$$\mathbf{C} = \begin{pmatrix} 0 & \rho & \tau & 0 \\ \rho & 0 & 0 & \tau \\ \tau & 0 & 0 & \rho \\ 0 & \tau & \rho & 0 \end{pmatrix}. \quad (\text{A5})$$

It can be set unitary by parameterizing

$$\tau = e^{i\alpha} \cos \beta, \quad \rho = ie^{i\alpha} \sin \beta. \quad (\text{A6})$$

with a pair of real parameters: the phase $\alpha \in [0, 2\pi]$, and the merit of background transparency $\beta \in [-\pi/2, \pi/2]$.

Then, by substituting Eqs. (A3) and (A5) into time reversal constraint $\mathbf{C}\mathbf{M}^* = -\mathbf{M}$ [Eq. (10) in the main text] one obtains for an even eigenstate:

$$m_{\text{even R}} = -m_{\text{even L}}^*(\tau + \rho), \quad m_{\text{even L}} = -m_{\text{even R}}^*(\tau + \rho), \quad (\text{A7})$$

while for an odd one, similarly using Eq. (A4) yields:

$$m_{\text{odd R}} = m_{\text{odd L}}^*(\tau - \rho), \quad m_{\text{odd L}} = m_{\text{odd R}}^*(\tau - \rho). \quad (\text{A8})$$

Substituting here the parameterization (A6) yields:

$$m_{\text{even L}} = -m_{\text{even R}}^* e^{i(\alpha+\beta)}, \quad (\text{A9})$$

$$m_{\text{odd L}} = m_{\text{odd R}}^* e^{i(\alpha-\beta)}. \quad (\text{A10})$$

Hereby we obtain an important very general restriction of the coupling parameters of modes of a planar membrane:

$$|m_{\text{even,odd R}}| = |m_{\text{even,odd L}}|, \quad (\text{A11})$$

i.e., regardless of their parity, they are coupled equally strongly to LCP and RCP waves.

Next, taking the diagonal elements of the matrix equation (11), allows relating the absolute values of the coupling parameters with the diagonal elements of the matrix Γ regardless of the mode parity:

$$\gamma_n = 2|m_{nR}|^2 = 2|m_{nL}|^2. \quad (\text{A12})$$

Finally, to express the complex phases, one can introduce the angles $\theta_{\text{even,odd}}$ and satisfy Eqs. (A9)–(A12) by setting:

$$m_{\text{even R}} = i\sqrt{\frac{\gamma_{\text{even}}}{2}}e^{i\frac{\alpha+\beta}{2}-i\theta_{\text{even}}}, \quad m_{\text{even L}} = i\sqrt{\frac{\gamma_{\text{even}}}{2}}e^{i\frac{\alpha+\beta}{2}+i\theta_{\text{even}}}, \quad (\text{A13})$$

$$m_{\text{odd R}} = \sqrt{\frac{\gamma_{\text{odd}}}{2}}e^{i\frac{\alpha-\beta}{2}-i\theta_{\text{odd}}}, \quad m_{\text{odd L}} = \sqrt{\frac{\gamma_{\text{odd}}}{2}}e^{i\frac{\alpha-\beta}{2}+i\theta_{\text{odd}}}. \quad (\text{A14})$$

Physically, the angles $\theta_{\text{even,odd}}$ characterize the direction of the the far-field polarization of the modes, as they actually are the angles between the linearly polarized electric field and the x -axis.

Appendix B: Port-orthogonal modes (opposite parity)

In some particular situations, the corresponding Hamiltonian \mathbf{H} can be chosen diagonal. The general precondition for this is the diagonal Γ in Eq. (11), which requires that any pair of modes n_1 and n_2 has to obey:

$$m_{n_1R}m_{n_2R}^* + m_{n_1L}m_{n_2L}^* + m'_{n_1R}m_{n_2R}^* + m'_{n_1L}m_{n_2L}^* = 0. \quad (\text{B1})$$

We will refer to this as a port-orthogonality condition.

It is easy to notice that by virtue of Eqs. (A3) and (A4), it is always fulfilled for the modes of different parity. For modes of the same parity, substituting Eqs. (A13) or (A14) reduces Eq. (B1) to

$$\cos(\theta_{n_1} - \theta_{n_2}) = 0 \quad (\text{B2})$$

i.e., to the orthogonality of their linear polarizations in the far field.

Apparently, the total number of port-orthogonal modes is restricted by the number of S-matrix channels, i.e., there can be maximum 2 odd and 2 even modes mutually orthogonal in the far field. As the corresponding Hamiltonian is diagonal, the matrix inversion in Eq. (12) is trivial and one obtains:

$$\mathbf{S} = \mathbf{C} - \sum_{n=1}^N \frac{1}{i(\omega - \omega_n) - \gamma_n} \begin{pmatrix} m_{nR}^2 & m_{nR}m_{nL} & m_{nR}m'_{nR} & m_{nR}m'_{nL} \\ m_{nL}m_{nR} & m_{nL}^2 & m_{nL}m'_{nR} & m_{nL}m'_{nL} \\ m'_{nR}m_{nR} & m'_{nR}m_{nL} & m'_{nR}{}^2 & m'_{nR}m'_{nL} \\ m'_{nL}m_{nR} & m'_{nL}m_{nL} & m'_{nL}m'_{nR} & m'_{nL}{}^2 \end{pmatrix} \quad (\text{B3})$$

1. Two-mode regime map

Figure 4 maps the cross-conversion dichroism (22) of two opposite-parity ($p_2 = -p_1$) resonances across the representative regimes of frequency detuning and linewidth mismatch discussed in Sec. III A.

Three limits organize the panels of Fig. 4. For degenerate modes of equal linewidth [$\omega_1 = \omega_2 = \omega_0$, $\gamma_1 = \gamma_2 = \gamma$, panel (a)] the dispersive term cancels and Eq. (22) collapses to a single Lorentzian,

$$\Delta T_{\text{cross}} = \text{sign}(p_1) \frac{\gamma^2}{\gamma^2 + (\omega - \omega_0)^2} \sin(2\beta) \sin(2\Delta\theta_{12}). \quad (\text{B4})$$

It is symmetric about resonance and bounded by $|\Delta T_{\text{cross}}| \leq 1$. The bound is reached at $\Delta\theta_{12} = \pm\pi/4$ and $\beta = \pm\pi/4$, a half-transparent background, $|\tau|^2 = 1/2$.

Keeping the modes degenerate but mismatching their linewidths [$\omega_1 = \omega_2 = \omega_0$, $\gamma_1 \gg \gamma_2$, panel (b)] turns the response into a dispersive *Fano* lineshape, antisymmetric in detuning about ω_0 and reaching $|\Delta T_{\text{cross}}| = 1$ at the half-transparent background $\beta = \pm\pi/4$.

Lifting the frequency degeneracy [panels (c) and (d)] resolves the two resonances at ω_1 and ω_2 (vertical dotted lines): the response splits into two features centered at ω_1 and ω_2 , each carrying the dispersive weight $\text{Im}(A_1 A_2^*)$ of Eq. (22) with overall sign $\text{sign}(p_1) \sin(2\Delta\theta_{12})$. They merge into the single Lorentzian of panel (a) once the splitting drops below $\tilde{\gamma}$.

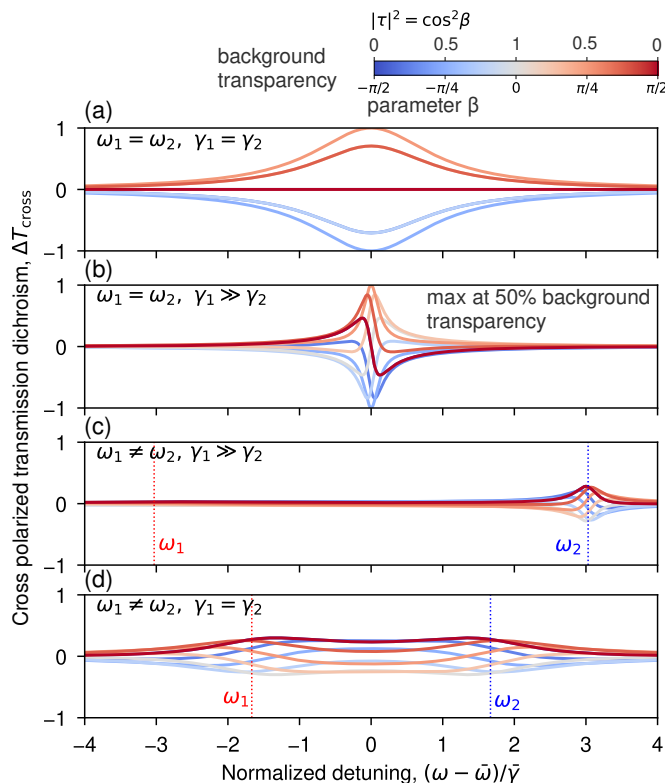


FIG. 4. **Cross-conversion dichroism of two opposite-parity resonances.** Two-mode model computed from Eq. (22). Dimensionless parameters are detuning $(\omega - \bar{\omega})/\bar{\gamma}$ with $\bar{\omega} = (\omega_1 + \omega_2)/2$ and $\bar{\gamma} = (\gamma_1 + \gamma_2)/2$. Each curve corresponds to a different background transmission $|\tau|^2 = \cos^2\beta$ (colorbar). Four representative parameter regimes are shown: (a) degenerate frequencies and equal linewidths ($\omega_1 = \omega_2, \gamma_1 = \gamma_2$); (b) degenerate frequencies with mismatched linewidths ($\gamma_1 \gg \gamma_2$); (c) non-degenerate frequencies with mismatched linewidths; and (d) non-degenerate frequencies with equal linewidths. Vertical dotted lines in (c) and (d) mark the individual resonance positions ω_1 (red) and ω_2 (blue).

Appendix C: Port-non-orthogonal modes (same parity)

Consider a pair of modes of the same parity and non-orthogonal far fields. For definiteness, we choose them to be even and denote them as 1 and 2, writing their eigenfrequencies as $\Omega_{1,2} = \omega_{1,2} - i\gamma_{1,2}$ and the coupling parameters as

$$m_{1,2R} = i\sqrt{\frac{\gamma_{1,2}}{2}} e^{i\frac{\alpha+\beta}{2} - i\theta_{1,2}}, \quad m_{1,2L} = i\sqrt{\frac{\gamma_{1,2}}{2}} e^{i\frac{\alpha+\beta}{2} + i\theta_{1,2}}, \quad (C1)$$

where the angles $\theta_{1,2}$ characterize the far-field directions. Substituting these coupling parameters into the off-diagonal element of the condition (11) and using the parity (A3) we obtain:

$$\gamma_{12} = \gamma_{21} = \sqrt{\gamma_1\gamma_2} \cos(\Delta\theta_{12}), \quad (C2)$$

where $\Delta\theta_{12} = \theta_1 - \theta_2$.

The corresponding Hamiltonian reads as:

$$\mathbf{H} = \begin{pmatrix} \Omega_1 & -i\gamma_{12} \\ -i\gamma_{12} & \Omega_2 \end{pmatrix}, \quad (C3)$$

and its non-diagonal form determines that, according to Eq. (7), even in the absence of external excitation, neither of the modes p_1 or p_2 evolves without mixing with the other. Therefore, they are not true eigenmodes in the classical sense, they are not those obtained by numerical eigenstate solvers or observed by the S-matrix poles in transmission and reflection. This is rarely discussed in the literature, but the fact itself is known for a long time, see e.g. [40].

To express the true modes, one resolves the Hamiltonian eigenfrequencies as:

$$\Omega_{\pm} = \frac{1}{2}(\Omega_1 + \Omega_2) \pm \sqrt{\frac{1}{4}(\Omega_1 - \Omega_2)^2 - \gamma_{12}^2}, \quad (C4)$$

and introduces the transformation matrix

$$\mathbf{T} = \frac{1}{D} \begin{pmatrix} -i(\Omega_2 - \Omega_+) & \gamma_{12} \\ \gamma_{12} & i(\Omega_2 - \Omega_+) \end{pmatrix} \quad (\text{C5})$$

with

$$D^2 = (\Omega_+ - \Omega_-)(\Omega_2 - \Omega_+). \quad (\text{C6})$$

which diagonalizes the Hamiltonian as

$$\mathbf{THT} = \tilde{\mathbf{H}}, \quad (\text{C7})$$

with

$$\tilde{\mathbf{H}} = \begin{pmatrix} \Omega_+ & 0 \\ 0 & \Omega_- \end{pmatrix}. \quad (\text{C8})$$

This transformation matrix is symmetric and orthogonal, so that $\mathbf{TT} = \mathbf{1}$, but it is not Hermitian which reflects the non-Hermitian character of the Hamiltonian.

Accordingly, one can transform the TCMT equations (7) and (9) to a new form with the diagonal Hamiltonian:

$$\frac{d\tilde{\mathbf{p}}}{dt} = i(\omega\mathbf{1} - \tilde{\mathbf{H}})\tilde{\mathbf{p}} + \tilde{\mathbf{M}}^T \mathbf{a}, \quad (\text{C9})$$

and

$$\mathbf{b} = \tilde{\mathbf{M}}\tilde{\mathbf{p}} + \mathbf{C}\mathbf{a} \quad (\text{C10})$$

with the vector of new mode amplitudes introduced as:

$$\tilde{\mathbf{p}} = \mathbf{T}\mathbf{p}. \quad (\text{C11})$$

and the new matrix of coupling parameters:

$$\tilde{\mathbf{M}} = \mathbf{M}\mathbf{T}. \quad (\text{C12})$$

This transformed set of CMT equations allows expressing the S-matrix in the form of Eq. (B3) explicitly describing the contributions of two resonances:

$$\mathbf{S} = \mathbf{C} - \frac{\mathbf{m}_+ \mathbf{m}_+^T}{i(\omega - \Omega_+)} - \frac{\mathbf{m}_- \mathbf{m}_-^T}{i(\omega - \Omega_-)}, \quad (\text{C13})$$

where the vectors of coupling parameters of the mixed modes constitute the coupling matrix:

$$\tilde{\mathbf{M}} = (\mathbf{m}_+, \mathbf{m}_-) = \begin{pmatrix} \tilde{m}_{+R} & \tilde{m}_{-R} \\ \tilde{m}_{+L} & \tilde{m}_{-L} \\ \tilde{m}_{+L} & \tilde{m}_{-L} \\ \tilde{m}_{+R} & \tilde{m}_{-R} \end{pmatrix}, \quad (\text{C14})$$

where

$$\tilde{m}_{+R,L} = \frac{1}{D} [-i(\Omega_2 - \Omega_+)m_{1R,L} + \gamma_{12}m_{2R,L}], \quad (\text{C15})$$

$$\tilde{m}_{-R,L} = \frac{1}{D} [\gamma_{12}m_{1R,L} + i(\Omega_2 - \Omega_+)m_{2R,L}], \quad (\text{C16})$$

where the parity-determined relations (A4) imposed the same restriction on the mixed modes: a mixture of odd modes is also odd. Non-Hermitian mode transformation \mathbf{T} does not preserve the mode energy. Accordingly, the relations (10) and (11) do not restrict the coupling parameters (C15) and (C16) and do not dictate the mixed modes to be linearly polarized in the far field. Elliptically and, eventually, circularly polarized modes become possible.

Expressing the S-matrix in the form (C13) allows, in particular, writing its components describing the cross-polarized transmission as:

$$t_{\text{RL}} = \frac{m_{\pm\text{L}}^2}{i(\omega - \Omega_+)} + \frac{m_{-\text{L}}^2}{i(\omega - \Omega_-)}, \quad (\text{C17})$$

$$t_{\text{LR}} = \frac{m_{\pm\text{R}}^2}{i(\omega - \Omega_+)} + \frac{m_{-\text{R}}^2}{i(\omega - \Omega_-)}. \quad (\text{C18})$$

For the resonances occurring at distinct frequencies, the peak resonant values of CD_{cross} (2) are directly determined by the modal contributions expressed by the modal circular dichroism [14]:

$$\text{CD}_{\text{cross}}^{\pm\text{mode}} = \frac{|m_{\pm\text{L}}|^4 - |m_{\pm\text{R}}|^4}{|m_{\pm\text{L}}|^4 + |m_{\pm\text{R}}|^4}. \quad (\text{C19})$$

However, as the coupling through radiative channels induces stronger difference in the mode decay rates rather than in their real frequencies, the actual situation is much more complex. To characterize a particular mode one can take the ellipticity of its far field, the Stokes parameter S_3 :

$$S_3^{\pm\text{mode}} = \frac{|m_{\pm\text{R}}|^2 - |m_{\pm\text{L}}|^2}{|m_{\pm\text{R}}|^2 + |m_{\pm\text{L}}|^2}. \quad (\text{C20})$$

as an indicator of the mode chirality. Both $\text{CD}_{\text{cross}}^{\pm\text{mode}}$ and $S_3^{\pm\text{mode}}$ reach their extreme ± 1 values when either of the coupling parameters vanishes.

It is truly remarkable that the conversion circular dichroism remains zero in the absence of dissipation loss even if one of the dressed modes eventually becomes circularly polarized. This general fact directly follows from the S-matrix form (C13), which has no contributions from the background to the coefficients of reflections r_{RR} and r_{LL} and transmissions t_{LR} and t_{RL} . As the dressed modes “ \pm ” inherit the same parity from the bare modes, the magnitudes of these coefficients are equal in pairs: $|t_{\text{LR}}| = |r_{\text{RR}}|$ and $|t_{\text{RL}}| = |r_{\text{LL}}|$. The energy conservation dictates that

$$1 = |t_{\text{LR}}|^2 + |t_{\text{RR}}|^2 + |r_{\text{RR}}|^2 + |r_{\text{LR}}|^2, \quad (\text{C21})$$

$$1 = |t_{\text{RL}}|^2 + |t_{\text{LL}}|^2 + |r_{\text{LL}}|^2 + |r_{\text{RL}}|^2, \quad (\text{C22})$$

where $r_{\text{LR}} = r_{\text{RL}}$ due to reciprocity and $t_{\text{RR}} = t_{\text{LL}}$ due to the membrane plane symmetry. Accordingly, the cross-polarized transmissions are bound to be equally strong $|t_{\text{RL}}|^2 = |t_{\text{LR}}|^2$. This is why only the mode combinations including those of different parity are considered in the Main text.

Appendix D: Numerical methods

Eigenmodes and spectra are obtained with the finite-element solver COMSOL Multiphysics (Wave Optics module, `ewfd`). A single unit cell with Floquet-periodic boundaries along x and y and perfectly matched layers along z represents the infinite membrane. An eigenfrequency study yields the complex eigenfrequencies $\Omega_n = \omega_n - i\gamma_n$ (conjugated to the $e^{-i\omega t}$ convention) and the modal fields \mathbf{E}_n .

The transmission amplitudes of the S-matrix (5) are computed with a background-field formulation. The background field is set to a circularly polarized (RCP or LCP) plane wave incident along $-z$, and the solver returns the resulting total field. The co- and cross-polarized transmission coefficients are obtained by projecting the field onto the circular basis (4) and averaging it over a transverse plane on the transmission side, placed a small gap before the PML so that only the propagating zeroth diffraction order contributes; normalizing to the incident amplitude gives $t_{\text{RR}}, t_{\text{LL}}, t_{\text{RL}}, t_{\text{LR}}$ and hence ΔT_{cross} (3).

Eqs. (A1)–(A2) for the up–down parity p_n can be compactly rewritten using the $z \rightarrow -z$ operator $\hat{\sigma}_h = \text{diag}(1, 1, -1)$ as [23]

$$\hat{\sigma}_h \mathbf{E}_n(\hat{\sigma}_h^{-1} \mathbf{r}) = p_n \mathbf{E}_n(\mathbf{r}). \quad (\text{D1})$$

We can convert this to the normalized overlap of a mode with its mirror image for the numerical calculation:

$$p_n = \frac{\int_V \hat{\sigma}_h \mathbf{E}_n(\hat{\sigma}_h^{-1} \mathbf{r}) \cdot \mathbf{E}_n(\mathbf{r}) dV}{\int_V \mathbf{E}_n(\mathbf{r}) \cdot \mathbf{E}_n(\mathbf{r}) dV}. \quad (\text{D2})$$

The integral runs over the membrane domain V , taken symmetric about $z = 0$. In COMSOL the mirrored field $\mathbf{E}_n(\hat{\sigma}_h^{-1} \mathbf{r})$ is evaluated with a General Extrusion operator implementing the map $(x, y, z) \rightarrow (x, y, -z)$, and the overlap with an integration coupling over V . The normal component $E_{n,z}$ enters with a minus sign, as dictated by $\hat{\sigma}_h$.